BNL-107214-2014-JA

Effect of surface termination on the electronic properties of $LaNiO_3$ films

Divine P. Kumah[1], Andrei Malashevich[1], Ankit S. Disa[1], Dario A. Arena[2], Fred J. Walker[1], Sohrab Ismail-Beigi[1], and Charles H. Ahn[1,3]

[1]Center for Research on Interface Structures and Phenomena
and Department of Applied Physics,
Yale University, New Haven, Connecticut 06520, USA

[2] National Synchrotron Light Source,
Brookhaven National Laboratory, Upton, New York 11973, USA

[3]Department of Mechanical Engineering and Materials Science,
Yale University, New Haven, Connecticut 06520, USA

Abstract

The electronic and structural properties of thin $LaNiO_3$ films grown using molecular beam epitaxy are studied as a function of the net ionic charge of the surface terminating layer. We demonstrate that electronic transport in nickelate heterostructures can be manipulated through changes in the surface termination due a strong coupling of the surface electrostatic properties to the structural properties of the Ni-O bonds that govern electronic conduction. We observe experimentally and from first principles theory an asymmetric response of the structural properties of the films to the sign of the surface charge, which results from a strong interplay between electrostatic and mechanical boundary conditions governing the system. The structural response results in ionic buckling in the near-surface NiO_2 planes for films terminated with negatively charged NiO_2 and bulk-like NiO_2 planes for films terminated with positively charged LaO planes. The ability to modify transport properties by the deposition of a single atomic layer can be used as a guiding principle for nanoscale device fabrication.

I. INTRODUCTION

Controlling and exploiting the polar nature of ionic materials has strong scientific and technical implications for determining the functional properties of materials for technological applications [1-11]. Polar interfaces and surfaces are most simply achieved by terminating a crystalline material along a lattice direction where the planes of ions have alternating signs of net charge. Polar insulating materials have been used to create long-ranged electrostatic effects that drive electronic or ionic reconstructions [12-14]. The use of a metallic (i.e. conducting) system with an ionic sublattice seems less likely to succeed because of screening from mobile charge carriers. Here, we show that this approach can in fact provide fresh opportunities for exploring and controlling structure-property relations. Within the screening length of the metal, uncompensated electric fields exist that create forces on the ions and lead to structural distortions. When the film thickness is of the same order as the screening length, one expects strong modification of the properties of the entire film. Moreover, we show that in ionic metals, the screening length is enhanced by almost an order of magnitude over the Thomas Fermi screening length. Understanding the structural-property relations in these systems is crucial for designing heterostructure devices for a wide range of applications including Mott field effect transistors and liquid ionic-gate electric double layer transistors [15-18]. Finally, since there are at least two choices of surface termination with opposite polarity, one can envisage nanoscale devices comprising of thin films of the same thickness but with strongly differing materials properties.

In this manuscript, we demonstrate that the surface termination of thin $LaNiO_3$ (LNO) films and the resulting screening response near the surface controls the coexistence of symmetry-breaking polar distortions and metallicity. Films with an equivalent number of NiO_2 planes show a metal-

insulator transition as a function of the surface terminating layer. In addition, we show how these differences stem from dissimilar screening behavior and structural distortions for the two polarities. We note that for bulk systems, the coexistence of a non-centrosymmetric polar crystal structure and metallicity is rare due to the ability of mobile carriers to effectively screen internal electric fields. Recent interest in such 'polar metals', first proposed by Anderson *et al.* [19], has been driven by the discovery of ferroelectric-like (polar) distortions in the metallic complex oxide $LiOsO_3$ [20, 21] and theoretical predictions of non-centrosymmetric layered metallic perovskite oxides [22]. Our work ties into these recent works by showing such effects at the atomic scale, demonstrating macroscopic consequences of the existence of polar distortions in conducting metal oxide systems.

Bulk LNO is a paramagnetic and metallic oxide with the centrosymmetric $R\bar{3}c$ space group. In thin film form, symmetry-lowering polar distortions occur in the top 3-4 surface unit cells (uc) of NiO_2-terminated LNO films, which arise in response to the uncompensated electric field induced at the surface of the film [23, 24]. This polar reconstruction results in the reduction of the overlap of the Ni e_g and O *2p* orbitals, leading to a thickness dependent metal-insulator transition [23-28]. Gross perturbations of the system, such as capping the LNO films with the polar insulator $LaAlO_3$, suppress the polar distortions by removing the surface field in the LNO and restore bulk-like Ni-O bonding and metallic conductivity [23]. Here, we exploit the ability to control materials composition with atomic layer precision to study the effect of changing a single terminating layer of LNO thin films and to elucidate the effect of the surface charge on the electronic and structural behavior of films within the electrostatic screening length. For the (001) LNO films considered here, this involves choosing between positively charged $(LaO)^+$ or negatively charge $(NiO_2)^-$ terminating layers. We find that films terminated with NiO_2 planes are

insulating, while films of comparable thicknesses terminated with LaO planes are metallic due to an in-equivalence in the structural responses to the direction of the induced surface field.

II. EXPERIMENT

The LNO films are grown using oxygen plasma-assisted molecular beam epitaxy on insulating AlO_2-terminated $LaAlO_3$ (LAO) substrates [23, 24]. NiO_2-terminated films are grown by co-depositing LaO and NiO_2. The LaO terminated films are fabricated by first co-depositing LaO and NiO_2, followed by the growth of a monolayer of LaO with the Ni shutter closed. Film thicknesses are calibrated *in situ* using reflection high energy electron diffraction [29]. LaO and NiO_2-terminated 3-4.5 uc thick films (a perovskite unit cell (uc) corresponds to a NiO_2-LaO bilayer) are deposited at a substrate temperature of 590°C in an oxygen plasma environment with a partial pressure of 5×10^{-6} Torr; the films are cooled in the plasma from the growth temperature to room temperature to ensure full oxygen stoichiometry. The film thicknesses and surface terminations are confirmed *ex situ* with synchrotron x-ray diffraction measurements. The roughness extracted from x-ray reflectivity fits is less than 1 unit cell, in agreement with atomic force microscopy measurements. In-plane transport measurements are carried out between 2 K and 300 K using the van der Pauw configuration with sputtered Au contacts.

To determine the atomic-scale structural properties of the LNO films as a function of the terminating layer, we perform synchrotron x-ray surface diffraction measurements along substrate-defined crystal truncation rods (CTRs). The experiments are performed in vacuum at 300 K for 3-4.5 uc thick films at the 33ID beamline at the Advanced Photon Source with an incident x-ray wavelength of 0.688 Å (18 keV). The diffracted intensities are measured using a solid state Pilatus area detector [30, 31]. X-ray absorption measurements of the nickelate films

are performed at the oxygen *K*-absorption edge at the U4B soft x-ray beamline at Brookhaven National Laboratory.

III. RESULTS

A. Transport Measurements

The measured resistivity versus temperature curves as a function of film thickness and termination are compared in Figure 1. The 3 and 4 uc thick films terminated with NiO_2 planes show insulating transport behavior, as characterized by an increase in the film resistivity with decreasing temperature. In contrast, the LaO-terminated films (3.5 uc and 4.5 uc) are metallic, with an order of magnitude lower resistivity and a slight upturn in resistivity below 50 K, characteristic of two-dimensional electronic transport [32, 33]. The transport properties of the metallic LaO-terminated films are similar to those of heterostructures comprised of 3 uc thick $LaNiO_3$ films capped with 6 uc thick $LaAlO_3$ layers [23].

One might expect that surface termination would not significantly affect transport properties: reversing polarity of the surface layer should reverse the sign of (i) the screening charge, (ii) the electric field distribution, and (iii) the electrostatic forces on the ions and thus the polar distortions. Transport in LNO films is controlled by the Ni-O bond lengths and the Ni-O-Ni bond angles, which in turn control Ni 3d – O 2p orbital overlap and thus electron motion in the lattice [23, 34, 35]. Therefore, reversed polar distortion patterns on an initially centrosymmetric structure should yield the same overall bond lengths and distortions and hence the same transport. Since the measured transport behavior differs from this scenario, an unexpected and substantive structural difference must be present between the two terminations. Structurally, the surface NiO_2 layer of the NiO_2-terminated film has a missing apical oxygen, while all the NiO_2

planes in the LaO-terminated film have full octahedral coordination. The differences in the Ni-coordination result in different mechanical boundary conditions for the two film terminations which should play a role in constraining the distortions induced by the surface field.

B. Atomic-Scale Structural Measurements

The atomic structure is derived from the CTRs using the coherent Bragg rod analysis (COBRA) method [13, 29, 36, 37]. The structural results for the NiO_2-terminated 3 uc film are in agreement with previously reported results showing a surface polar distortion involving relative oxygen displacements away from the film-vacuum interface relative to the cation positions [23, 24]. Figures 2(a) and 2(b) show slices through the COBRA-derived electron density maps along the [1 1 0] and [1 0 0] directions, respectively, for the LaO-terminated 3.5 uc LNO film. For the LaO-terminated film, oxygen displacements are observed towards the film-vacuum interface in the top two LaO layers in Figure 2(a), leading to a net film dipole moment opposite to that observed for the NiO_2-terminated film. The opposite dipole moment for the two surface terminations is consistent with the opposite signs of the charge of the terminating layer and the resulting surface electric fields. The COBRA-derived structures are refined [38] to determine the in-plane Ni-O-Ni bond angles. For the LaO, film, the average film in-plane Ni-O-Ni bond angles are determined from the fit to be $165^o \pm 3^o$. for the LaO-terminated film, in agreement with values for bulk $LaNiO_3$ (165°) [39] and thin $LaNiO_3$ films capped with $LaAlO_3$. For the NiO_2 terminated film, the measured surface bond angle is $153^o \pm 5^o$.

C. Theoretical Results

In contrast to the NiO_2-terminated film, where polar distortions are observed in both LaO and NiO_2 planes, Figure 2(b) shows no rumpling of the NiO_2 planes for the LaO-terminated film. To explain this discrepancy, we perform density-functional theory (DFT) calculations to determine the relaxed ground state atomic structures of 3 uc LNO films on LAO substrates for both NiO_2 and LaO terminations. Calculations use the *ab initio* supercell plane-wave approach with the Quantum-ESPRESSO code package [40, 41], the local density approximation (LDA) [42], and ultrasoft pseudopotentials [43]. Additional theoretical details [44, 45] are provided in the supplementary materials [29]. This theoretical approach predicts atomic-scale structures for nickelate systems that agree quantitatively with experiment [23]. Figures 3(a) and 3(b) show the predicted structures for the NiO_2 and LaO-terminated films, respectively. Both films exhibit a strong rumpling of the cations and anions in the film growth [001] direction. The direction of these polar distortions is determined by the direction of the surface field due to the non-zero net formal charge of the terminating layers. The net induced dipole moment depends on the surface termination and points towards (away from) the substrate for the positively (negatively) charged LaO (NiO_2) surface. We quantify the magnitude of the polar distortion in each atomic plane via the difference in cation and anion z coordinates, i.e. z_{Cation}-z_O, which is shown in Figures 3(c) and 3(d) for the two terminations and compared with the experimentally measured values. For the NiO_2 termination, polar rumpling occurs in both LaO and NiO_2 planes, with decaying amplitude going in from the surface. In contrast, for LaO termination, the polar displacements occur only in the LaO planes with undistorted NiO_2 planes. The absence of polar distortions in the NiO_2 planes for LaO-terminated films maintains bulk-like Ni-O bonding and explains the enhanced metallic transport measured by experiment, in contrast to the intuitively expected symmetric behavior.

We note that, a critical difference between the LaO-terminated film and films capped with 6 uc-thick $LaAlO_3$ is that, while a significant surface field exists in the LaO-terminated film due to the polar discontinuity at the film-vacuum interface, the absence of a polar-discontinuity at the $LaNiO_3$-$LaAlO_3$ interface removes the field in the $LaAlO_3$-capped films [23]. Hence, no polar distortions are observed in the $LaAlO_3$-capped films while the field present in the LaO-terminated films leads to the observed distortions in the LaO planes.

IV. DISCUSSION

The striking aspect of the results in Figure 2 and Figure 3 is how the structure of the NiO_2 planes in the LaO-terminated films are essentially undistorted, compared to the ~0.23 Å distortion in the topmost NiO_2 layer of the NiO_2-terminated film. An understanding of the inequivalence of the electronic transport and structure for the two terminations requires knowledge of the mechanical constraints on the bond distortions through the atomic force constant matrix. We compute the interatomic spring constants and find that the largest spring constants connect Ni and the apical O along their bond vector. Inclusion of the Ni-O spring constant couples the Ni and O displacements: in the case of LaO termination, the force on the surface apical O is in the [0 0 1] direction towards the vacuum and is large in magnitude. Thus, the surface apical O on the LaO-terminated surface pulls the Ni below it strongly upwards. This upward mechanical force counteracts the force on the subsurface NiO_2 layer due to the near surface electric field (the surface field moves the Ni+ ions downward), resulting in a bulk-like in-plane Ni-O bond angle. For the NiO_2-terminated surface where the apical oxygen is missing for the surface NiO_2 layer, a mechanical force imbalance on the Ni arises from the absence of an apical ion for the topmost Ni ion. The broken Ni-apical O bond leads to a reduced mechanical force to counteract the upward

motion of the Ni ion induced by the surface field, resulting in the observed rumpling of the NiO_2 planes. In the perovskite lattice, the La ions are weakly bonded to the O ions, leading to the observed rumpling in the LaO planes. Screening of the polar field due to mobile charge in each layer also contributes to the observed structures, as detailed in the Supplementary Materials [29].

The coexistence of metallicity and polar distortions over many atomic layers is unexpected, since mobile carriers can effectively screen imposed fields. In metals where mobile electrons cause screening, the Thomas-Fermi framework is used to describe the screening response of an electron gas to external perturbations. For bulk $LaNiO_3$ with one mobile electron per perovskite cell, a simple textbook estimate of the Thomas-Fermi screening length is 1 Å [46]. However, the polarization profiles computed by theory in Figure 3 (and measured by experiment, Figure 2, and in Ref. [23]) point to an enlarged screening length, requiring a generalized Thomas-Fermi model, where the additional screening due to the response of the ionic sublattice (and associated bound electrons) is taken into account. The ionic response screens an imposed external potential such that the mobile carriers see a reduced external perturbation. The net effect is to increase the screening length by a factor $\sqrt{\varepsilon}$, where ε is the dielectric constant for the insulating ionic sublattice. A reasonable estimate of $\varepsilon \sim 25$ yields a screening length of ~ 5 Å for $LaNiO_3$, which is in good accord with the above results. The thickness of these films is thus on the order of the screening length, leading to the coexistence of metallic and polar behavior.

The predicted inequivalence in the polar distortions between terminations should also manifest itself as an increased Ni-O orbital overlap for LaO-terminated films. We characterize the effect of the surface termination on the Ni-O hybridization by performing x-ray absorption measurements at the oxygen *K*-absorption edge at the U4B soft x-ray beamline at Brookhaven

National Laboratory. The measured total electron yield spectra for the LaO and NiO_2-terminated films at 300 K are shown in Figure 4. The incident x-rays are linearly polarized with the polarization vector parallel to the sample surface. The intensity of the pre-peak at ~530 eV is associated with the degree of Ni 3*d*–O 2*p* hybridization, where increased hybridization is correlated with increased metallicity [47, 48]. The inset of Figure 4 shows a comparison of the pre-peak intensities for insulating NiO_2-terminated 3 and 4 uc films and a metallic LaO-terminated 3 uc film. In comparison with the insulating NiO_2-terminated films, we find a 25% increase in the integrated pre-peak intensity for the LaO-terminated film, consistent with the observed metallic transport properties and the increased hybridization expected from the reduced polar distortions observed in the atomic structures; however, the reduced surface coordination may also contribute to the reduced pre-peak intensity.

V. CONCLUSION

In conclusion, we have demonstrated experimentally and theoretically how the surface termination of ultrathin nickelate films couples to polar structural distortions, leading to significant changes in electronic conduction. We find that 3 and 4 uc LNO films terminated with LaO are metallic with polar distortions confined to LaO planes, while 3 uc films capped with NiO_2 are insulating with polar distortions occurring in both the LaO and NiO_2 planes. XAS measurements, synchrotron-based structural measurements, and theoretical calculations show that the surface polarization plays a critical role in determining the structural distortions in the NiO_2 planes and hence the electronic transport. The inequivalent structural response to the direction of the surface field may play a role in clarifying the observed differences in the critical thickness for metallic LNO films and band properties measured using angle-resolved

photoemission spectra [27, 28]. Future work should consider the effect of tuning the mechanical boundary conditions by the addition of non-polar capping layers. The coexistence of induced polar non-centrosymmetric distortions and metallicity within the enlarged screening length of the LaO-terminated LNO films provides a general route to induce non-bulk structural distortions in nanoscale metallic oxide systems in order to modify and control their macroscopic properties.

Recent interest in ultra-thin oxide materials as alternate channel materials for device applications has arisen due to their inherently high carrier densities, as well as the strong coupling of their electronic and magnetic order parameters to structural degrees of freedom [1, 15, 17, 49-52]. The ability to use the charge of the surface termination to determine the structural and transport properties of ultra-thin oxide films provides a route to switch the properties of correlated oxide materials for applications including logic, memory and sensors. In addition, the ability to modify the transport properties of thin oxide films by an order of magnitude by the deposition of a single atomic layer is expected to have strong implications for aggressive device scaling and for nanotechnology device architecture and processing schemes [53]. For example, complex circuitry can be achieved by capping regions of an insulating NiO_2 terminated film with an atomic layer LaO, potentially reducing additional processing steps for electrode fabrication.

ACKNOWLEDGMENTS

Work at Yale is supported by NSF MRSEC DMR-1119826 (CRISP). Use of the Advanced Photon Source is supported by the U.S. Department of Energy, Office of Science, Office of Basic Energy Sciences, under Contract No. DE-AC02–06CH11357. Use of the National Synchrotron Light Source, Brookhaven National Laboratory, is supported by the U.S. Department of Energy, Office of Science, Office of Basic Energy Sciences, under Contract No.

DE-AC02–98CH10886. Partial personnel and facilities support is provided by NSF grant CNS 08–21132 and by the facilities and staff of the Yale University Faculty of Arts and Sciences High Performance Computing Center. Additional computations are carried out via the NSF XSEDE resources through grant TG-MCA08X007.

Figures

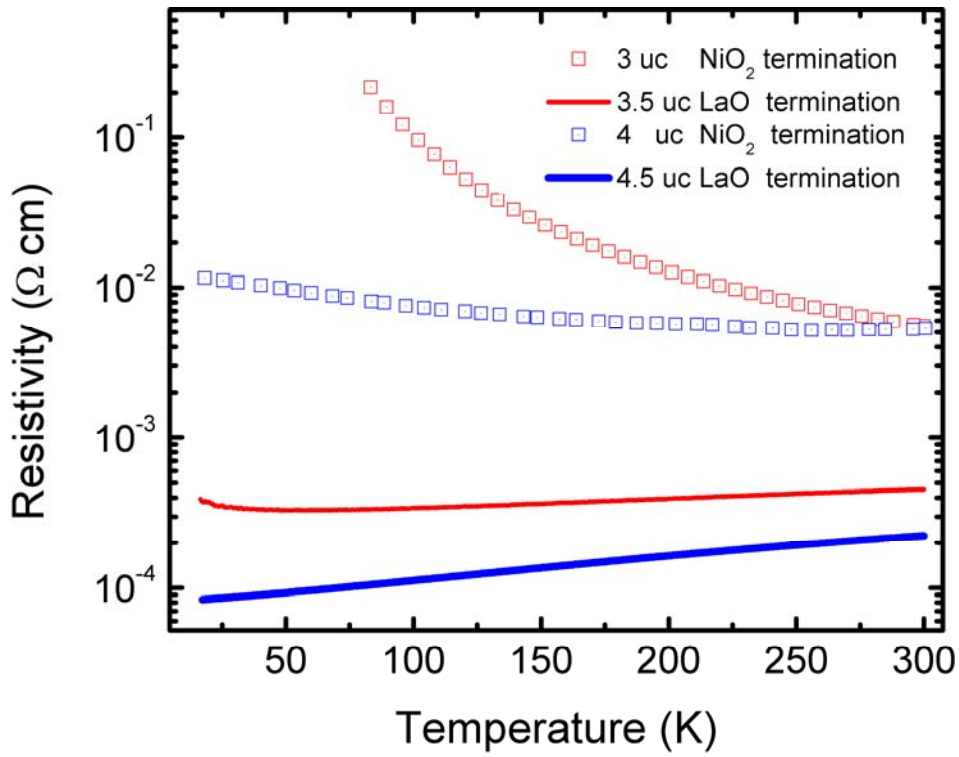

.

Figure 1: Temperature dependent transport measurements for $LaNiO_3$ films as a function of surface termination and film thickness (a perovskite unit cell (uc) corresponds to a NiO_2-LaO bilayer). Films terminated with LaO (solid curves) are metallic, and films terminated with NiO_2 (squares) are insulating.

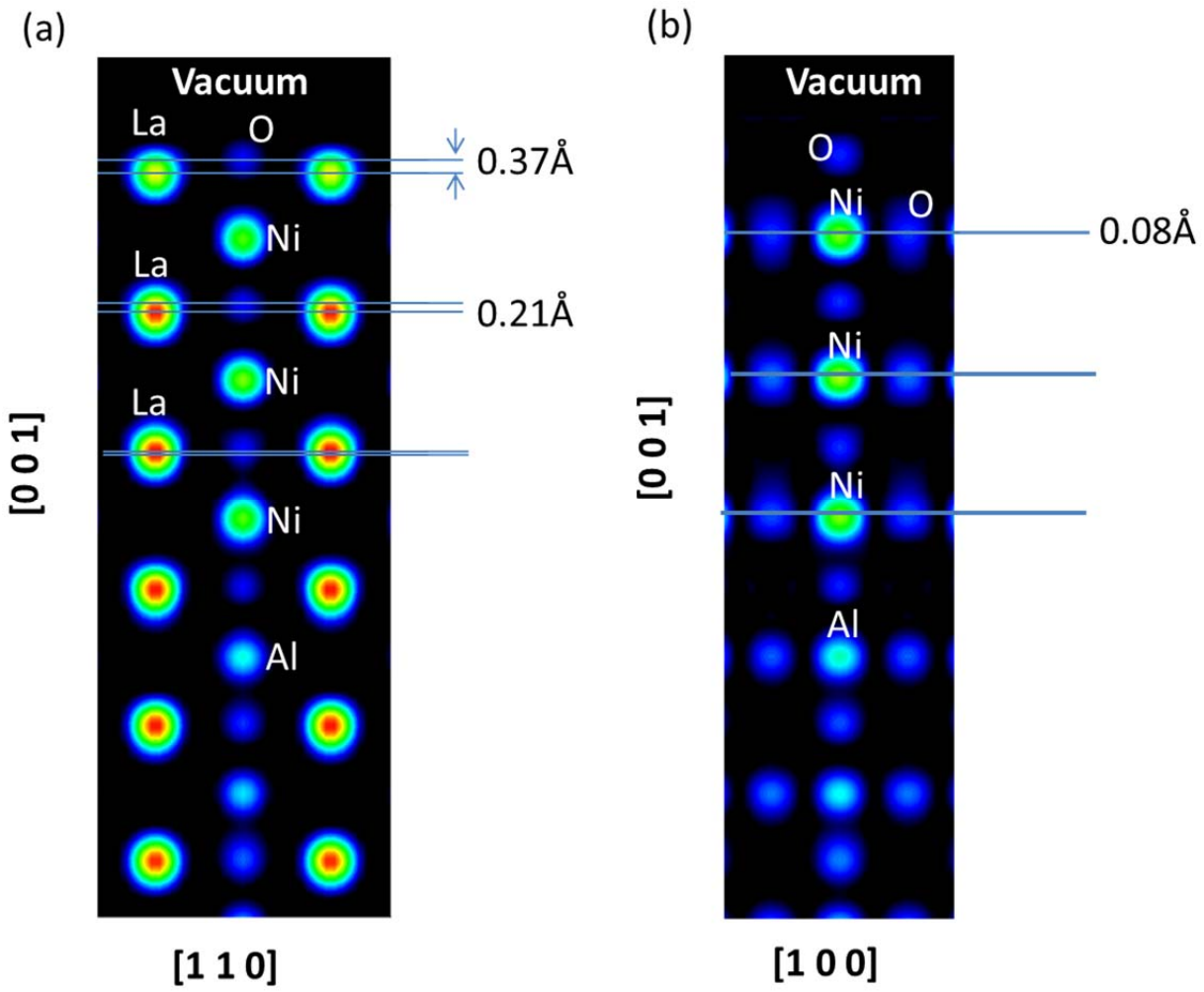

Figure 2: Vertical cuts through experimentally determined COBRA-derived electron density maps along (a) [1 1 0] and (b) [1 0 0] directions for a 3.5 unit cell thick $LaNiO_3$ film terminated with LaO. The horizontal lines indicate the centers of mass in the vertical direction of the cation and anion positions.

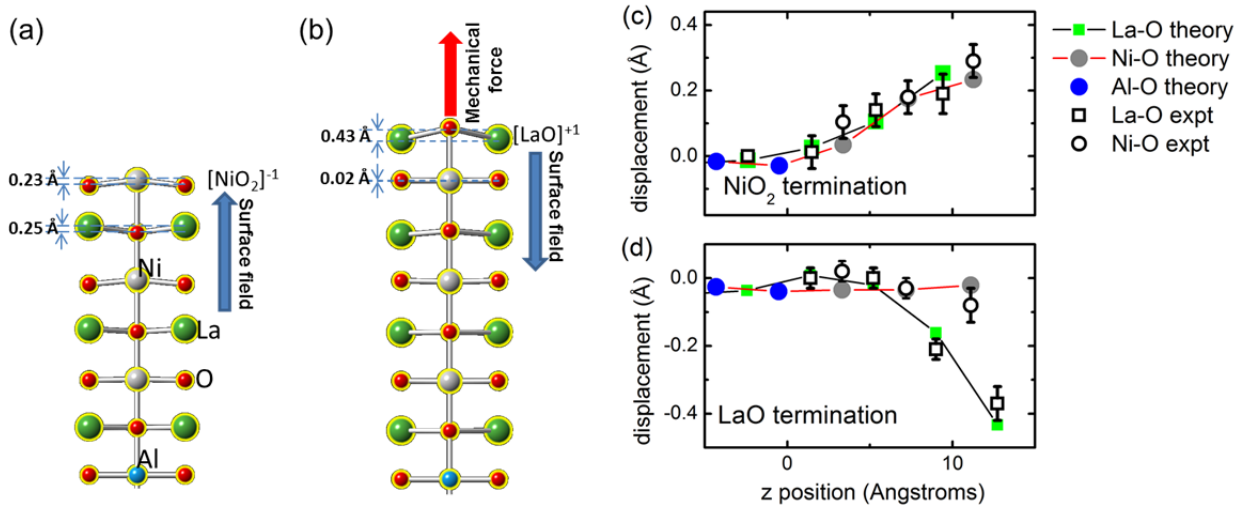

Figure 3: Theoretically predicted structures for (a) 3 uc NiO_2 and (b) 3.5 uc LaO-terminated $LaNiO_3$ films epitaxially strained to $LaAlO_3$ substrates. The blue arrows indicate the direction of the surface fields due to the nominal charge of the termination layer. The red arrow indicates the direction of the mechanical force exerted by the apical oxygen on the Ni ion below it. Layer-resolved cation-anion displacements are shown for (c) NiO_2 and (d) LaO-terminated films. The film-substrate interface is at z=0. Positive displacement indicates cation movement towards the vacuum compared to oxygen in the same layer. The solid lines are shown as a guide to the eye. Experimentally measured displacements are shown as open symbols.

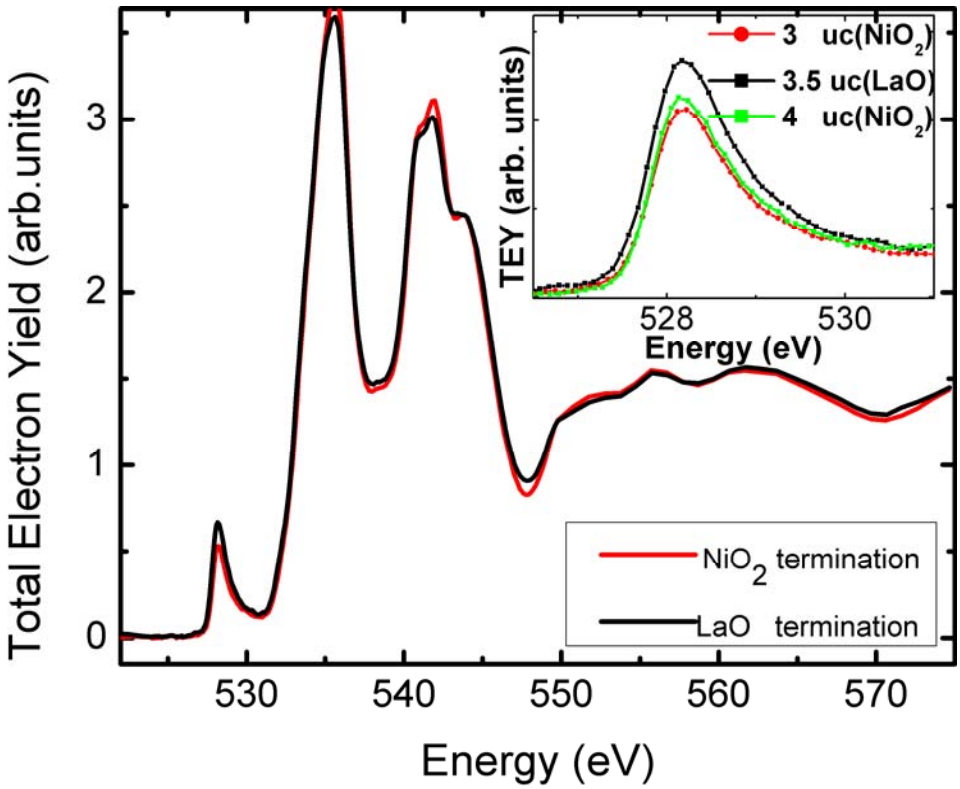

Figure 4: Oxygen-*K* edge absorption spectra for 3.5 uc (LaO terminated) and 3 uc (NiO_2-terminated) thick $LaNiO_3$ films grown on (001) oriented $LaAlO_3$ substrates. The inset shows a comparison of the pre-peak intensities for 3-4 uc LNO films. The surface terminations are indicated in parenthesis.

[1] H. Hwang, Y. Iwasa, M. Kawasaki, B. Keimer, N. Nagaosa, and Y. Tokura, Emergent phenomena at oxide interfaces, Nat. Mater. **11**, 103 (2012).
[2] J. Goniakowski, F. Finocchi, and C. Noguera, Polarity of oxide surfaces and nanostructures, Rep. Prog. Phys. **71**, 016501 (2008).
[3] H. Chen, A. M. Kolpak, and S. Ismail-Beigi, Fundamental asymmetry in interfacial electronic reconstruction between insulating oxides: an ab initio study, Phys. Rev. B **79**, 161402 (2009).
[4] P. Zubko, S. Gariglio, M. Gabay, P. Ghosez, and J.-M. Triscone, Interface Physics in Complex Oxide Heterostructures, Annual Review of Condensed Matter Physics **2**, 141 (2011).
[5] V. K. Lazarov, S. A. Chambers, and M. Gajdardziska-Josifovska, Polar oxide interface stabilization by formation of metallic nanocrystals, Phys. Rev. Lett. **90**, 216108 (2003).
[6] J. Burton, and E. Tsymbal, Evolution of the band alignment at polar oxide interfaces, Phys. Rev. B **82**, 161407 (2010).
[7] R. Ramesh, and N. A. Spaldin, Multiferroics: progress and prospects in thin films, Nat. Mater. **6**, 21 (2007).
[8] V. E. Henrich, The surfaces of metal oxides, Rep. Prog. Phys. **48**, 1481 (1985).
[9] J. Chakhalian, A. Millis, and J. Rondinelli, Whither the oxide interface, Nat. Mater. **11**, 92 (2012).
[10] M. Dawber, K. Rabe, and J. Scott, Physics of thin-film ferroelectric oxides, Rev. Mod. Phys. **77**, 1083 (2005).
[11] S.-W. Cheong, and M. Mostovoy, Multiferroics: a magnetic twist for ferroelectricity, Nat. Mater. **6**, 13 (2007).
[12] R. Pentcheva, and W. E. Pickett, Electronic phenomena at complex oxide interfaces: insights from first principles, J. Phys. Condens. Matter **22**, 043001 (2010).
[13] P. R. Willmott, S. A. Pauli, R. Herger, C. M. Schlepütz, D. Martoccia, B. D. Patterson, B. Delley, R. Clarke, D. Kumah, C. Cionca, and Y. Yacoby, Structural Basis for the Conducting Interface between $LaAlO_3$ and $SrTiO_3$, Phys. Rev. Lett. **99**, 155502 (2007).
[14] J. Lee, and A. A. Demkov, Charge origin and localization at the n-type SrTiO 3/LaAlO 3 interface, Phys. Rev. B **78**, 193104 (2008).
[15] C. Ahn, A. Bhattacharya, M. Di Ventra, J. Eckstein, C. D. Frisbie, M. Gershenson, A. Goldman, I. Inoue, J. Mannhart, and A. J. Millis, Electrostatic modification of novel materials, Rev. Mod. Phys. **78**, 1185 (2006).
[16] R. Scherwitzl, P. Zubko, I. G. Lezama, S. Ono, A. F. Morpurgo, G. Catalan, and J.-M. Triscone, Electric-Field Control of the Metal-Insulator Transition in Ultrathin $NdNiO_3$ Films, Adv. Mater. **22**, 5517 (2010).
[17] P. Moetakef, T. A. Cain, D. G. Ouellette, J. Y. Zhang, D. O. Klenov, A. Janotti, C. G. Van de Walle, S. Rajan, S. J. Allen, and S. Stemmer, Electrostatic carrier doping of GdTiO3/SrTiO3 interfaces, Appl. Phys. Lett. **99**, 232116 (2011).
[18] J. Ye, S. Inoue, K. Kobayashi, Y. Kasahara, H. Yuan, H. Shimotani, and Y. Iwasa, Liquid-gated interface superconductivity on an atomically flat film, Nat. Mater. **9**, 125 (2010).
[19] P. Anderson, and E. Blount, Symmetry Considerations on Martensitic Transformations:" Ferroelectric" Metals?, Phys. Rev. Lett. **14**, 217 (1965).
[20] Y. Shi, Y. Guo, X. Wang, A. J. Princep, D. Khalyavin, P. Manuel, Y. Michiue, A. Sato, K. Tsuda, and S. Yu, A ferroelectric-like structural transition in a metal, Nat. Mater. **12**, 1024 (2013).
[21] V. Keppens, Structural transitions:'Ferroelectricity'in a metal, Nat. Mater. **12**, 952 (2013).
[22] D. Puggioni, and J. M. Rondinelli, Designing a robustly metallic noncenstrosymmetric ruthenate oxide with large thermopower anisotropy, Nat. Comm. **5**, 3432 (2014).

[23] D. P. Kumah, A. S. Disa, J. H. Ngai, H. Chen, A. Malashevich, J. W. Reiner, S. Ismail-Beigi, F.-J. Walker, and C. H. Ahn, Tuning the Structure of Nickelates to Achieve Two-Dimensional Electron Conduction, Adv. Mater. **26**, 1935 (2014).
[24] H. Chen, D. P. Kumah, A. S. Disa, F. J. Walker, C. H. Ahn, and S. Ismail-Beigi, Modifying the Electronic Orbitals of Nickelate Heterostructures via Structural Distortions, Phys. Rev. Lett. **110**, 186402 (2013).
[25] J. Son, P. Moetakef, J. M. LeBeau, D. Ouellette, L. Balents, S. J. Allen, and S. Stemmer, Low-dimensional Mott material: Transport in ultrathin epitaxial $LaNiO_3$ films, Appl. Phys. Lett. **96**, 062114 (2010).
[26] R. Scherwitzl, S. Gariglio, M. Gabay, P. Zubko, M. Gibert, and J. M. Triscone, Metal-Insulator Transition in Ultrathin $LaNiO_3$ Films, Phys. Rev. Lett. **106**, 246403 (2011).
[27] E. Sakai, M. Tamamitsu, K. Yoshimatsu, S. Okamoto, K. Horiba, M. Oshima, and H. Kumigashira, Gradual localization of Ni 3d states in $LaNiO_3$ ultrathin films induced by dimensional crossover, Phys. Rev. B **87**, 075132 (2013).
[28] P. King, H. Wei, Y. Nie, M. Uchida, C. Adamo, S. Zhu, X. He, I. Božović, D. Schlom, and K. Shen, Atomic-scale control of competing electronic phases in ultrathin LaNiO3, Nat. Nano. **9**, 443 (2014).
[29] See Supplemental Material at [URL will be inserted by publisher] for addtional experimental and theoretical details.
[30] B. Henrich, A. Bergamaschi, C. Broennimann, R. Dinapoli, E. Eikenberry, I. Johnson, M. Kobas, P. Kraft, A. Mozzanica, and B. Schmitt, PILATUS: A single photon counting pixel detector for X-ray applications, Nucl. Instrum. Meth. A **607**, 247 (2009).
[31] C. Schleputz, R. Herger, P. Willmott, B. Patterson, O. Bunk, C. Bronnimann, B. Henrich, G. Hulsen, and E. Eikenberry, Improved data acquisition in grazing-incidence X-ray scattering experiments using a pixel detector, Acta Cryst. A **61**, 418 (2005).
[32] P. A. Lee, and T. V. Ramakrishnan, Disordered electronic systems, Rev. Mod. Phys. **57**, 287 (1985).
[33] B. Altshuler, A. Aronov, and P. Lee, Interaction Effects in Disordered Fermi Systems in Two Dimensions, Phys. Rev. Lett. **44**, 1288 (1980).
[34] J. Torrance, P. Lacorre, A. Nazzal, E. Ansaldo, and C. Niedermayer, Systematic study of insulator-metal transitions in perovskites $RNiO_3$ (R=Pr,Nd,Sm,Eu) due to closing of charge-transfer gap, Phys. Rev. B **45**, 8209 (1992).
[35] J. Chakhalian, J. Rondinelli, J. Liu, B. Gray, M. Kareev, E. Moon, N. Prasai, J. Cohn, M. Varela, I. Tung, M. Bedzyk, S. Altendorf, F. Strigari, B. Dabrowski, L. Tjeng, P. Ryan, and J. Freeland, Asymmetric Orbital-Lattice Interactions in Ultrathin Correlated Oxide Films, Phys. Rev. Lett. **107**, 116805 (2011).
[36] D. Fong, C. Cionca, Y. Yacoby, G. Stephenson, J. Eastman, P. Fuoss, S. Streiffer, C. Thompson, R. Clarke, and R. Pindak, Direct structural determination in ultrathin ferroelectric films by analysis of synchrotron x-ray scattering measurements, Phys. Rev. B **71**, 144112 (2005).
[37] Y. Yacoby, M. Sowwan, E. Stern, J. O. Cross, D. Brewe, R. Pindak, J. Pitney, E. M. Dufresne, and R. Clarke, Direct determination of epitaxial interface structure in Gd2O3 passivation of GaAs, Nature Mater. **1**, 99 (2002).
[38] M. Bjorck, and G. Andersson, GenX: an extensible X-ray reflectivity refinement program utilizing differential evolution, J. of Appl. Cryst. **40**, 1174 (2007).
[39] J. L. Garcia-Munoz, J. Rodriguez-Carvajal, P. Lacorre, and J. B. Torrance, Neutron-diffraction study of $RNiO_3$ (R=La,Pr,Nd,Sm): Electronically induced structural changes across the metal-insulator transition, Phys. Rev. B **46**, 4414 (1992).

[40] M. C. Payne, M. P. Teter, D. C. Allan, T. A. Arias, and J. D. Joannopoulos, Iterative minimization techniques for ab initio total-energy calculations: molecular dynamics and conjugate gradients, Rev. Mod. Phys. **64**, 1045 (1992).
[41] P. Giannozzi, S. Baroni, N. Bonini, M. Calandra, R. Car, C. Cavazzoni, D. Ceresoli, G. L. Chiarotti, M. Cococcioni, and I. Dabo, QUANTUM ESPRESSO: a modular and open-source software project for quantum simulations of materials, Journal of Physics: Condensed Matter **21**, 395502 (2009).
[42] W. Kohn, and L. J. Sham, Self-Consistent Equations Including Exchange and Correlation Effects, Phys. Rev. **140**, A1133 (1965).
[43] D. Vanderbilt, Soft self-consistent pseudopotentials in a generalized eigenvalue formalism, Phys. Rev. B **41**, 7892 (1990).
[44] L. Bengtsson, Dipole correction for surface supercell calculations, Phys. Rev. B **59**, 12301 (1999).
[45] P. O. Löwdin, On the non-orthogonality problem connected with the use of atomic wave functions in the theory of molecules and crystals, The Journal of Chemical Physics **18**, 365 (1950).
[46] N. W. Ashcroft, and N. D. Mermin, Solid State Phys, Saunders, Philadelphia (1976).
[47] M. Medarde, A. Fontaine, J. L. García-Muñoz, J. Rodríguez-Carvajal, M. de Santis, M. Sacchi, G. Rossi, and P. Lacorre, $RNiO_3$ perovskites (R=Pr,Nd): Nickel valence and the metal-insulator transition investigated by x-ray-absorption spectroscopy, Phys. Rev. B **46**, 14975 (1992).
[48] A. S. Disa, D. P. Kumah, J. H. Ngai, E. D. Specht, D. A. Arena, F. J. Walker, and C. H. Ahn, Phase diagram of compressively strained nickelate thin films, APL Materials **1**, 032110 (2013).
[49] J. Mannhart, and D. Schlom, Oxide interfaces—an opportunity for electronics, Science **327**, 1607 (2010).
[50] D. Newns, J. Misewich, C. Tsuei, A. Gupta, B. Scott, and A. Schrott, Mott transition field effect transistor, Appl. Phys. Lett. **73**, 780 (1998).
[51] C. A. F. Vaz, J. Hoffman, Y. Segal, J. W. Reiner, R. D. Grober, Z. Zhang, C. H. Ahn, and F. J. Walker, Origin of the Magnetoelectric Coupling Effect in Pb(Zr0.2Ti0.8)O-3/La0.8Sr0.2MnO3 Multiferroic Heterostructures, Phys. Rev. Lett. **104**, 127202 (2010).
[52] A. Cavalleri, T. Dekorsy, H. H. Chong, J.-C. Kieffer, and R. W. Schoenlein, Evidence for a structurally-driven insulator-to-metal transition in VO 2: A view from the ultrafast timescale, Phys. Rev. B **70**, 161102 (2004).
[53] International Technology Roadmap for Semiconductors; http://www.itrs.net.

Supplementary Materials for
"Effect of surface termination on the electronic properties of $LaNiO_3$ films"

Divine P. Kumah[1], Andrei Malashevich[1], Ankit S. Disa[1], Dario A. Arena[2], Fred J. Walker[1], Sohrab Ismail-Beigi[1], and Charles H. Ahn[1,3]

[1]Center for Research on Interface Structures and Phenomena
and Department of Applied Physics,
Yale University, New Haven, Connecticut 06520, USA

[2] National Synchrotron Light Source,
Brookhaven National Laboratory, Upton, New York 11973, USA

[3]Department of Mechanical Engineering and Materials Science,
Yale University, New Haven, Connecticut 06520, USA

Computational Methods

The theoretical calculations in this work are carried out using density-functional theory (DFT) within the local-density approximation (LDA) [1] as implemented in Quantum ESPRESSO code package [2, 3]. We use Vanderbilt ultrasoft pseudopotentials [4] in the following reference configurations: La $5s^2 5p^6 5d^1 6s^{1.5} 6p^{0.5}$ ($r_c^s = r_c^d = 2.2a_0$, $r_c^p = 2.0a_0$), Ni $3d^8 4s^2 4p^0$ ($r_c^s = 2.03a_0$, $r_c^p = 2.23a_0$, $r_c^d = 2.0a_0$), Al $3s^2 3p^1$ ($r_c^s = r_c^p = 1.77a_0$, and O $2s^2 2p^4$ ($r_c^s = r_c^p = 1.3a_0$), where a_0 is the Bohr radius. The planewave kinetic energy and charge density cutoffs are 35 Ry and 280 Ry, respectively. The $LaNiO_3$ thin films are modeled by constructing supercells in a slab geometry, which contain (001)-oriented $LaNiO_3$ films with 3 NiO_2 layers (with different surface terminations) on top of the $LaAlO_3$ substrate with 4 AlO_2 layers (see Figure S1). The slabs are separated by ~20 Å, which we find to be sufficient to ensure that the spurious electric field in the vacuum region is negligible. We also check that there are no parasitic effects from electric field in the vacuum by comparing the results to those obtained with the dipole correction technique [5]. The majority of the calculations in this work are performed using the 1×1 in-plane

periodicity of the supercells. By performing several calculations with centered 2×2 supercells, we find that the polar distortions at the surface are essentially the same as in the case of 1×1 supercells. For Brilloin zone integrations in case of 1×1 supercells, we use a 6×6 k-point mesh and Gaussian smearing with 5 mRy smearing width. The in-plane lattice constant are fixed to the theoretically calculated bulk $LaAlO_3$ lattice constant in ideal perovskite configuration (3.71 Å). The structural relaxations were performed until the forces on all atoms became smaller than 3 meV/ Å.

Since the $LaAlO_3$ substrate is modeled by a relatively thin layer, to enforce bulk-like geometry, the atomic positions in the bottom three surface layers of $LaAlO_3$ are fixed to bulk values, while the positions of remaining atoms are optimized. The modeled substrate also has an artificial bottom surface (see Figure S1) which potentially could have an effect on the $LaNiO_3$ film. To check what role the bottom surface of the substrate plays on polar distortions at the surface of $LaNiO_3$, in addition to the AlO_2 termination of the $LaAlO_3$ (shown in Figure S1), we considered LaO termination by removing the bottom AlO_2 layer from each of the structures shown in Figure S1. We find that the surface geometry of $LaNiO_3$ film is insensitive to the surface termination of $LaAlO_3$. Moreover, we performed calculations on thicker $LaNiO_3$ films (up to 10 unit cells) and on symmetric $LaNiO_3$ slabs in vacuum up to 20 unit cells. In all cases we found that the polar distortions at the surface of $LaNiO_3$ film remain the same, thus proving that this is entirely a surface effect and the substrate has no effect (other than the in-plane compressive strain) on the surface geometry of $LaNiO_3$ film.

Screening Effects

The polar termination and resulting field on the (001) surface of the $LaNiO_3$ film leads to the accumulation of screening charge on the surface. Using density-functional theory (DFT), we estimate the amount of accumulated charge for both terminations by computing the electron occupation of Löwdin atomic orbitals [6] on each atom in the fully relaxed $LaNiO_3$ film and then subtract that occupation from the reference value for the same orbital in bulk $LaNiO_3$. Summing over all orbitals of each atom gives an accumulated screening charge on that atom. The results of these calculations for atoms in the top two unit cells are shown in Figure S2. We observe accumulation of negative charge (electrons) on the surface of NiO_2-terminated films and positive charge (holes) on the surface of LaO-terminated films, as expected. The amount of excess charge decays quickly going from the surface into the interior, which sets the scale of the screening length. Looking at the very top atomic layer of each film, one observes that more charge per unit cell accumulates in the top layer of the NiO_2-terminated film (-0.21*e* per primitive surface unit cell) than in the top layer of the LaO-terminated film (+0.15*e* per primitive surface cell). This observation is consistent with the NiO_2 layer being more effective at screening external perturbations compared to the LaO layer. Notice that while there is almost no excess charge in the La atoms, as expected for a closed-shell La^{3+} ion, there is some excess charge on the O^{2-} ions. This result is not surprising because O 2*p* states hybridize with the Ni 3*d* states, forming the e_g bands that cross the Fermi level.

Hellmann-Feynman forces

Poor screening in the LaO layers should lead to stronger polar fields at the top of the LaO-terminated film compared to the NiO_2-terminated film. Correspondingly, the forces acting on the

atoms on the surface of the LaO-terminated film in the ideal perovskite configuration (unrelaxed) are also expected to be stronger. To verify this scenario, we calculate the Hellmann-Feynman forces on atoms of the $LaNiO_3$ films in their unrelaxed structure for both terminations. The computed forces are shown schematically in Figures S3(a) and S3(b) for the NiO_2-terminated and LaO-terminated films, respectively. The forces on the terminating LaO layer in Figure S3(b) are observed to be twice as large as the forces on the NiO_2 terminating layer in Figure S3(a).

Growth details

The LNO films are grown using molecular beam epitaxy on AlO_2-terminated $LaAlO_3$ substrates as described in the main text. The film thicknesses are monitored in-situ using reflective high energy electron diffraction (RHEED). Figure S4 shows the intensity of the specular RHEED reflection as a function of growth time for 3 uc (NiO_2-termination) and 3.5 uc (LaO-termination) LNO films. The growth of both films begins with co-deposition of 3 monolayers of LaO and NiO_2 to obtain a 3 uc thick NiO_2-terminated films. To achieve LaO termination, the Ni shutter is closed and a monolayer of LaO is deposited. Figure S5 (a) and (b) show atomic force microscope images of the NiO_2 and LaO-terminated films respectively. Atomically smooth, unit cell high steps are observed which are identical to the morphology of the initial $LaAlO_3$ substrates.

Structural analysis

The diffracted intensities are analyzed using the coherent Bragg rod analysis (COBRA) technique. Figure S6 shows the COBRA-derived electron density map for the 3uc NiO_2-terminated $LaNiO_3$ film from which the experimental polar displacements in Figure 3(c) of the main text are extracted. Figure S7 shows the COBRA-converged fits obtained for the 3 uc $LaNiO_3$ film terminated with LaO. The atomic positions are extracted from the centers of mass

of the atomic peaks in the COBRA-derived electron density maps and refined using the GenX differential evolution fitting program [7]. The atomic Debye-Waller factors and the octahedral rotations are refined in the fits with the cation positions and the centers of mass of the anions fixed to the COBRA-derived positions. The average film in-plane Ni-O-Ni bond angles are determined from the fit to be 165 $^{o}\pm$ 3°. for the LaO-terminated film, in agreement with bulk $LaNiO_3$ and thin $LaNiO_3$ films capped with $LaAlO_3$ [8].

References

[1] W. Kohn, and L. J. Sham, Self-Consistent Equations Including Exchange and Correlation Effects, Phys. Rev. **140**, A1133 (1965).

[2] M. C. Payne, M. P. Teter, D. C. Allan, T. A. Arias, and J. D. Joannopoulos, Iterative minimization techniques for ab initio total-energy calculations: molecular dynamics and conjugate gradients, Rev. Mod. Phys. **64**, 1045 (1992).

[3] P. Giannozzi, S. Baroni, N. Bonini, M. Calandra, R. Car, C. Cavazzoni, D. Ceresoli, G. L. Chiarotti, M. Cococcioni, and I. Dabo, QUANTUM ESPRESSO: a modular and open-source software project for quantum simulations of materials, Journal of Physics: Condensed Matter **21**, 395502 (2009).

[4] D. Vanderbilt, Soft self-consistent pseudopotentials in a generalized eigenvalue formalism, Phys. Rev. B **41**, 7892 (1990).

[5] L. Bengtsson, Dipole correction for surface supercell calculations, Phys. Rev. B **59**, 12301 (1999).

[6] P. O. Löwdin, On the non-orthogonality problem connected with the use of atomic wave functions in the theory of molecules and crystals, The Journal of Chemical Physics **18**, 365 (1950).

[7] M. Bjorck, and G. Andersson, GenX: an extensible X-ray reflectivity refinement program utilizing differential evolution, J. of Appl. Cryst. **40**, 1174 (2007).

[8] D. P. Kumah, A. S. Disa, J. H. Ngai, H. Chen, A. Malashevich, J. W. Reiner, S. Ismail-Beigi, F.-J. Walker, and C. H. Ahn, Tuning the Structure of Nickelates to Achieve Two-Dimensional Electron Conduction, Adv. Mater. **26**, 1935 (2014).

Figures

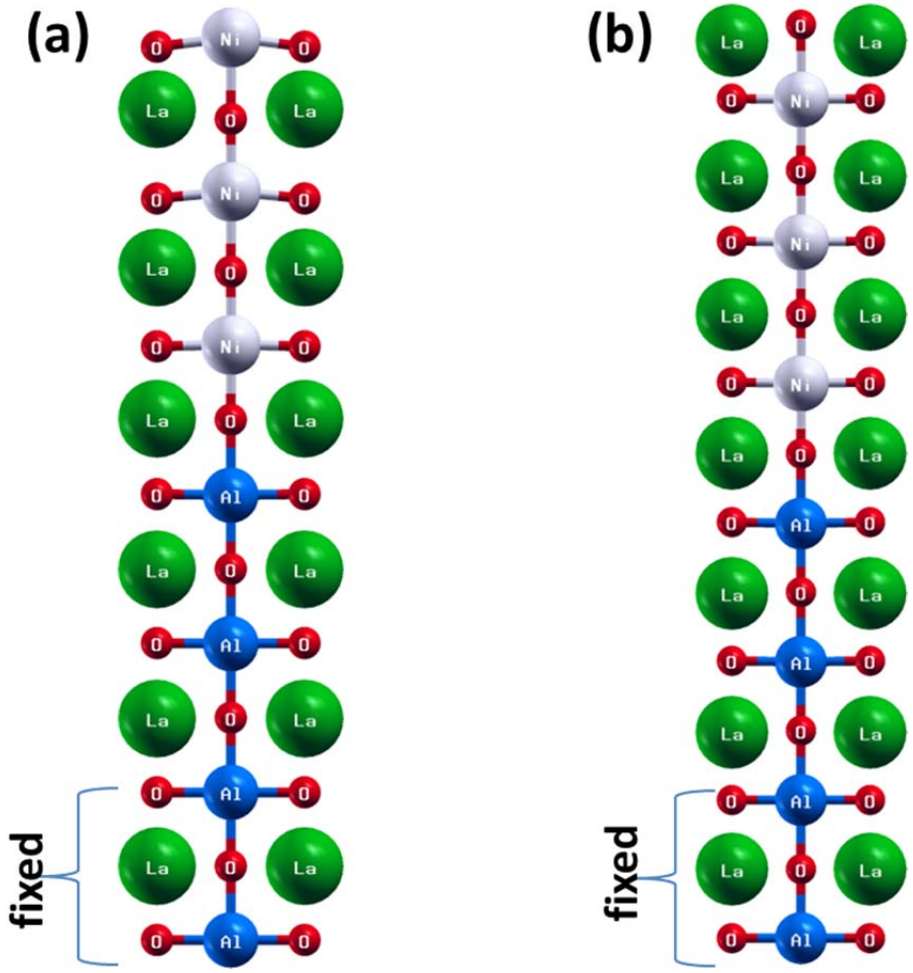

Figure S1: Theoretical 1×1 supercell used for calculating the structural properties of (a) NiO_2-terminate and (b) LaO-terminated $LaNiO_3$ films epitaxially strained to $LaAlO_3$. The slabs are separated by ~20 Å of vacuum, which we find to be sufficient to ensure that the spurious electric field in the vacuum region is negligible. The atomic postions for the bottom 3 monolayers of the $LaAlO_3$ substrate are constrained to bulk values.

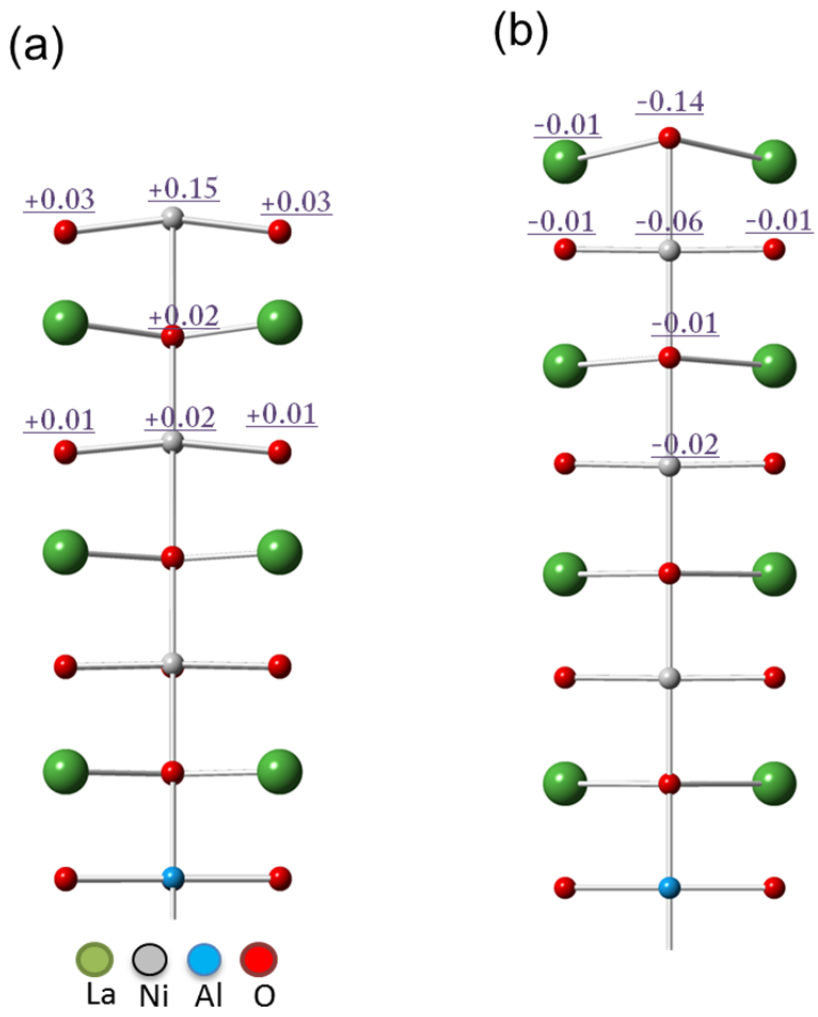

Figure S2: Excess charges (in units of *e*) computed theoretically using Löwdin orbital occupations for the atoms near the surface of 3 uc thick $LaNiO_3$ films on $LaAlO_3$ substrates with (a) NiO_2 and (b) LaO surface terminations. Positive (negative) charge values show hole (electron) accumulation. The vacuum interface is at the top in each panel.

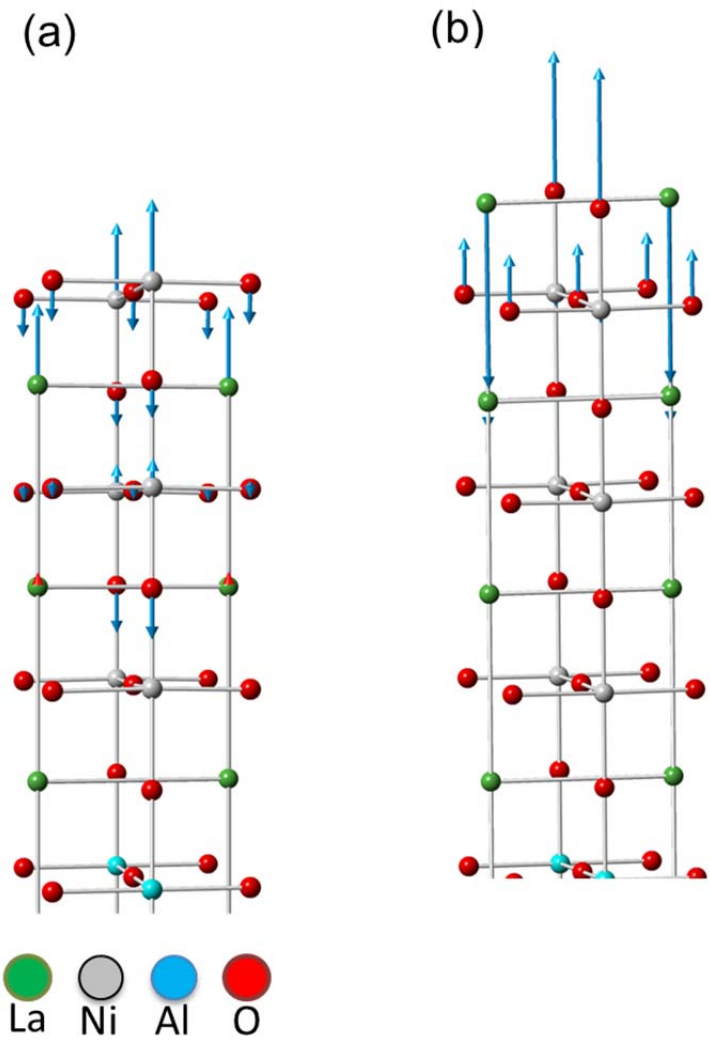

Figure S3: Computed Hellman-Feynman forces for (a) NiO_2 and (b) LaO-terminated $LaNiO_3$ films. The arrows indicate the direction and amplitudes of the computed forces on each atom.

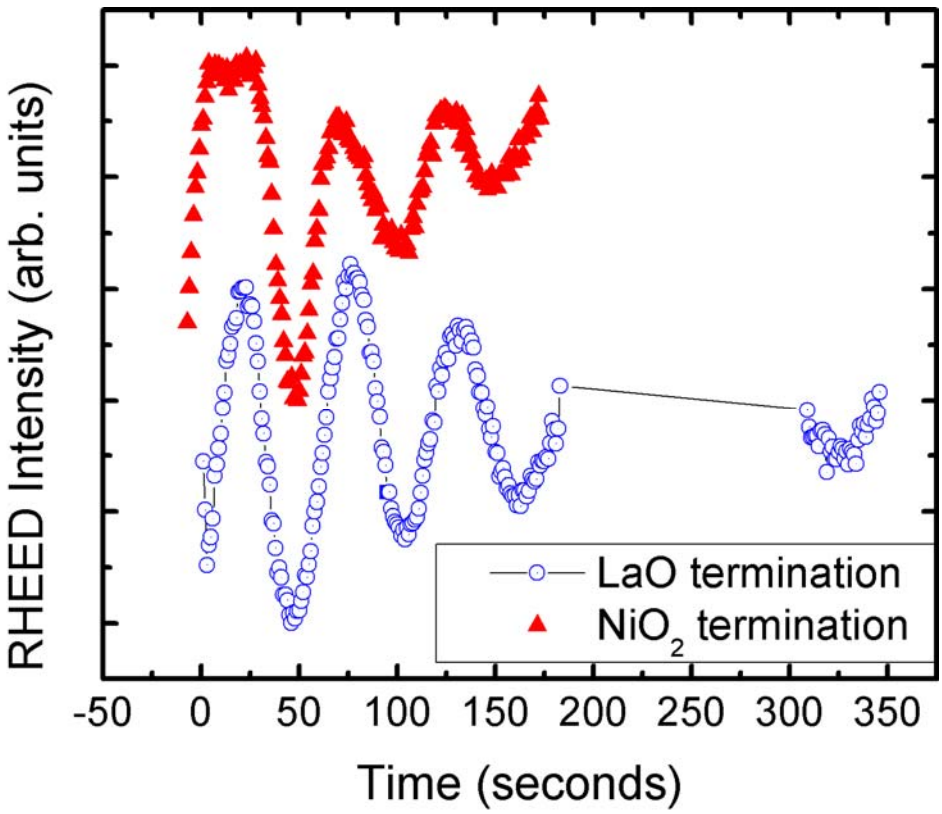

Figure S4: Oscillations of the RHEED specular intensity during the growth of a 3 uc thick NiO_2 terminated $LaNiO_3$ film (red triangles) by the codepostion of LaO and NiO_2 on AlO_2-terminated $LaAlO_3$ substrates. The LaO-terminated film(blue circles) follows the same initial growth sequence as the NiO_2 terminated film, however, the co-deposition is stopped after the deposition of 3 uc of $LaNiO_3$, the Ni shutter is closed (after 180 seconds) followed by the deposition of a monolayer of LaO.

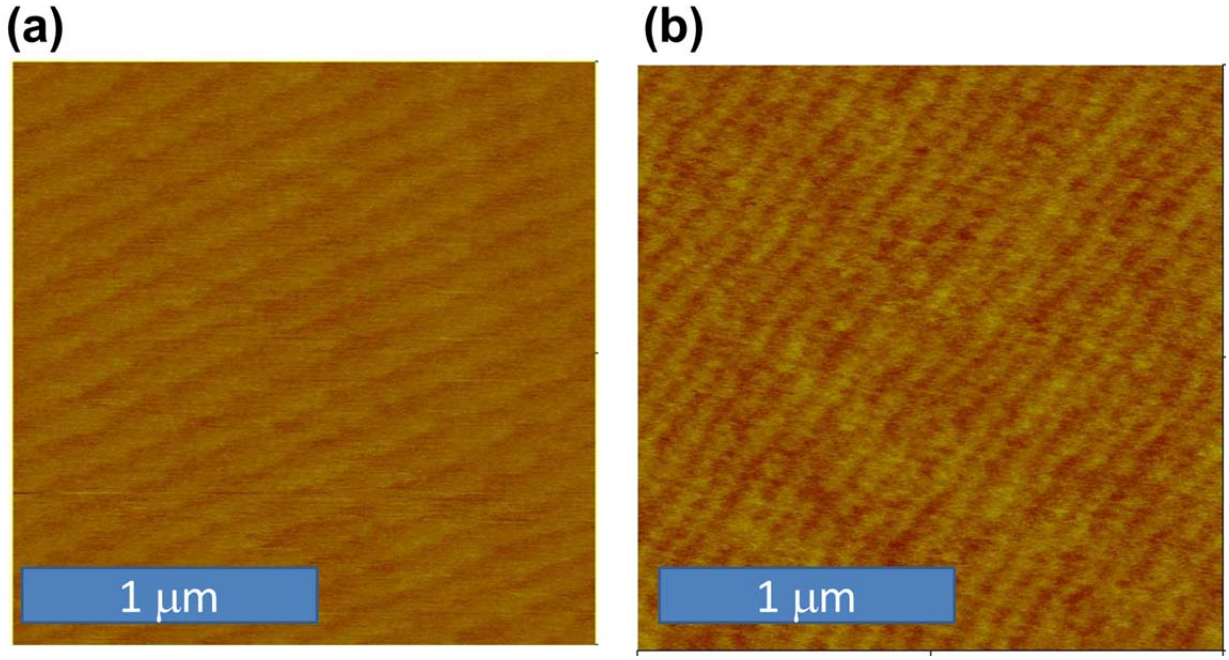

Figure S5: Atomic force measurements of 3 uc $LaNiO_3$ films terminated with (a) NiO_2 and (b) LaO deposited on AlO_2-terminated $LaAlO_3$ substrates. The average roughness is 0.1 nm. Unit cell high steps are visible on both film surfaces. The scale bar represents 1 um.

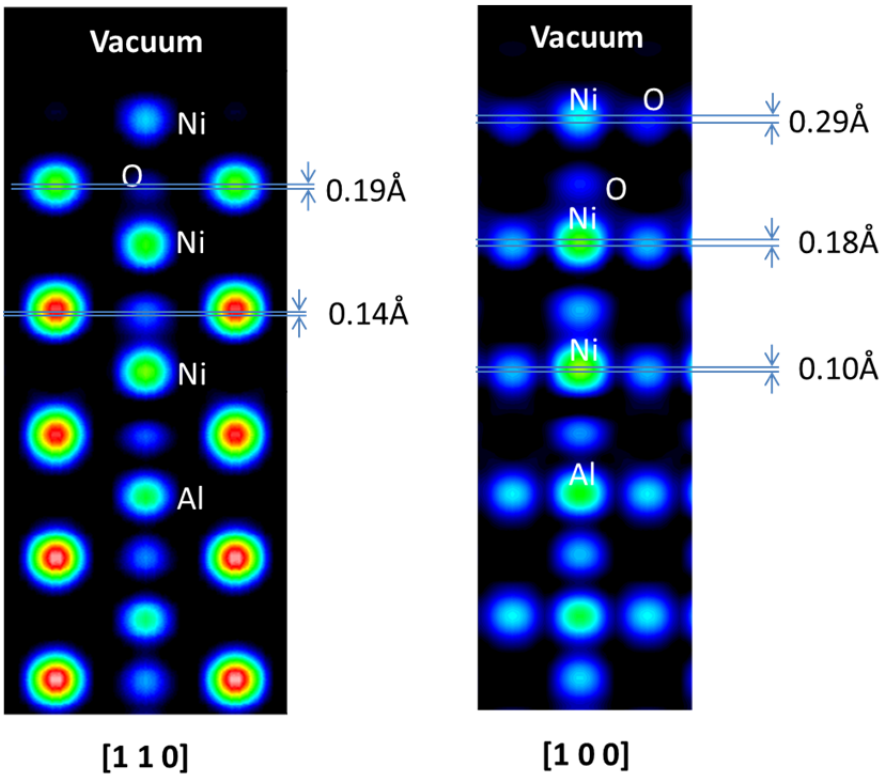

Figure S6: Vertical cuts through experimentally determined COBRA-derived electron density maps along (a) [1 1 0] and (b) [1 0 0] directions for a 3 uc thick $LaNiO_3$ film terminated with NiO_2. The horizontal lines indicate the centers of mass in the vertical direction of the cation and anion positions.

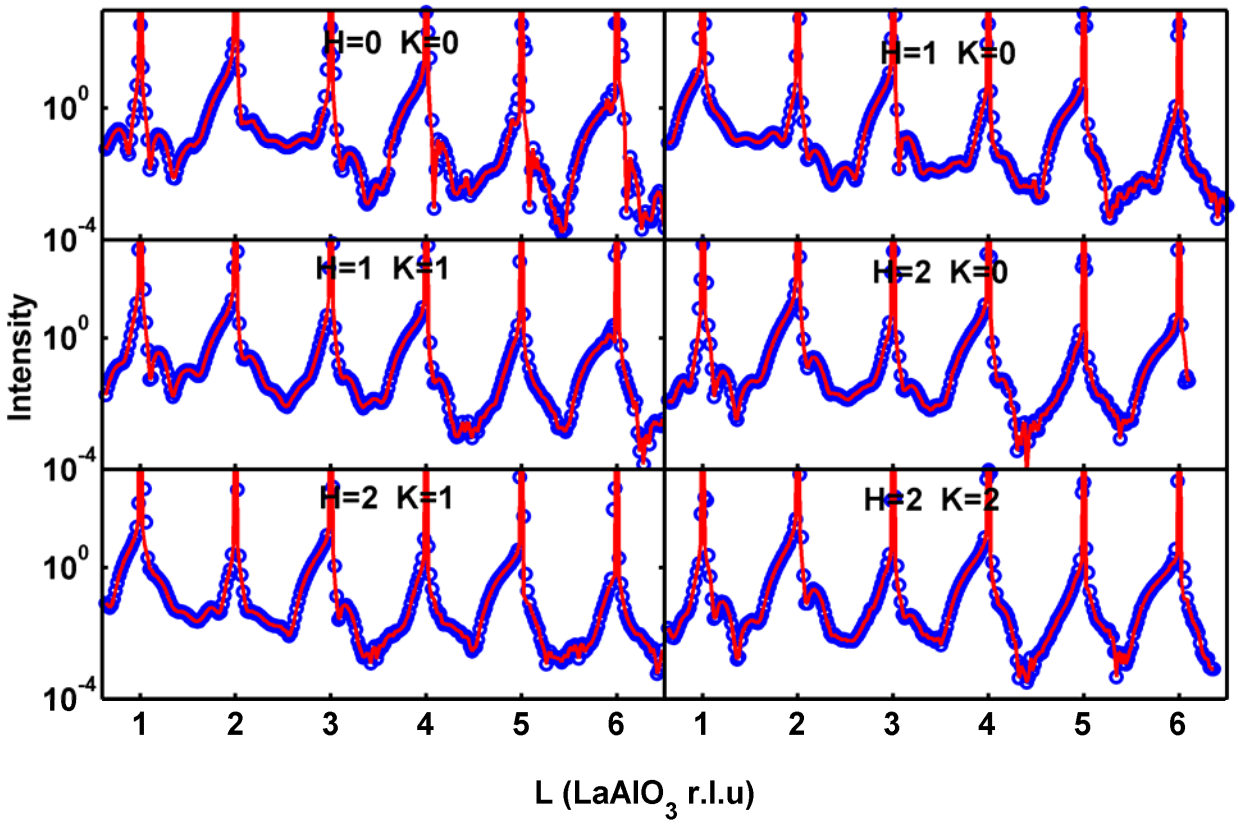

Figure S7: Measured crystal truncation rods (blue circles) and calculated crystal truncation rods for the COBRA-derived structure (solid red line) for a 3 uc LaO-terminated $LaNiO_3$ thin film grown on $LaAlO_3$.